Study of the reaction mechanisms of ^{136}Xe + p and ^{136}Xe + ^{12}C at 1 A GeV with inverse kinematics and large-acceptance detectors

Thomas Gorbinet, Orlin Yordanov, Jean-Eric Ducret, Thomas Aumann, Yassid Ayyad, Sébastien Bianchin, Olga Borodina, Alain Boudard, Christoph Caesar, Enrique Casarejos, et al.

▶ **To cite this version:**

Thomas Gorbinet, Orlin Yordanov, Jean-Eric Ducret, Thomas Aumann, Yassid Ayyad, et al.. Study of the reaction mechanisms of ^{136}Xe + p and ^{136}Xe + ^{12}C at 1 A GeV with inverse kinematics and large-acceptance detectors. Eur.Phys.J.A, 2019, 55 (1), pp.11. 10.1140/epja/i2019-12683-8 . cea-02536367

HAL Id: cea-02536367

https://cea.hal.science/cea-02536367

Submitted on 8 Apr 2020

HAL is a multi-disciplinary open access archive for the deposit and dissemination of scientific research documents, whether they are published or not. The documents may come from teaching and research institutions in France or abroad, or from public or private research centers.

L'archive ouverte pluridisciplinaire **HAL**, est destinée au dépôt et à la diffusion de documents scientifiques de niveau recherche, publiés ou non, émanant des établissements d'enseignement et de recherche français ou étrangers, des laboratoires publics ou privés.

Study of the reaction mechanisms of ^{136}Xe + p and ^{136}Xe +^{12} C at 1A GeV with inverse kinematics and large-acceptance detectors *

Thomas Gorbinet[1], Orlin Yordanov[2], Jean-Eric Ducret[1,3,4,5],†
Thomas Aumann[6,7], Yassid Ayyad[8]‡, Sébastien Bianchin[7],
Olga Borodina[7], Alain Boudard[1], Christoph Caesar[7],
Enrique Casarejos[9], Bronislaw Czech[10], Stanislav Hlavac[11],
Josef Klimo[11], Nikolaus Kurz[7], Christoph Langer[7],
Tudy Le Bleis[7], Sylvie Leray[1], Jerzy Lukasik[10],
Davide Mancusi[12], Piotr Pawlowski[10], Stéphane Pietri[7],
Christopher Rappold[6], Marie-Delphine Salsac[1]§,
Haik Simon[7], Martin Veselsky[11]

[1]DRF/IRFU/Département de Physique Nucléaire, CEA-Saclay,
F-91191 Gif-sur-Yvette, France
[2]Institute of Nuclear Research and Nuclear Energy, Bulgarian Academy of Sciences,
Tsarigradsko Chaussee, 72, BG-1784 Sofia, Bulgaria
[3]DRF/IRFU/Département d'Astrophysique, CEA-Saclay,
F-91191 Gif-sur-Yvette, France
[4]Centre Lasers Intenses et Applications, UMR 5106 CEA CNRS Université de Bordeaux,
F-33405 Talence, France
[5]GANIL, Boulevard Henri Becquerel, BP 55027, F-14076 Caen, France
[6]Institut für Kernphysik, Technische Universität Darmstadt,
D-64289 Darmstadt, Germany
[7]GSI Helmholtzzentrum für Schwerionenforschung, Planckstrasse 1,
D-64291 Darmstadt, Germany
[8]University of Santiago de Compostella, E-15782, S. de Compostella, Spain
[9]University of Vigo, E-36310 Vigo, Pontevedra, Spain
[10]Institute of Nuclear Physics, Polish Academy of Sciences,
ul. Radzikowskiego 152, PL-31-342 Krakow, Poland
[11]Institute of Physics, Slovak Academy of Sciences, Dubravska cesta 9,
SL-845 11 Bratislava, Slovak Republic
[12]DEN-Service d'études des réacteurs et de mathématiques appliquées (SERMA),
CEA, Université Paris-Saclay, F-91191, Gif-sur-Yvette, France

April 7, 2020

Abstract

The reactions ^{136}Xe + p and ^{136}Xe +^{12} C have been studied in inverse kinematics at 1 A GeV with the SPALADiN setup at GSI. The detection in coincidence of the final-state charged particles (projectile residues, nuclei of charge $Z \geq 2$) and neutrons was performed with a big-aperture dipole magnet and large-acceptance detectors. This provided an extended coverage of the phase space of decay products of the prefragment formed at the end of the intranuclear cascade. This coincidence measurement, performed on an event-by-event basis permits both an estimate of the excitation energy of the prefragments and a determination of their deexcitation channels. The element-production cross sections are compared with existing data and theoretical models. The evolution of observables such as the total multiplicity or the fragment production with the prefragment's excitation energy is studied for both reactions and compared with models.

PACS: *25.40.Sc*-Spallation reactions, *24.10.-i*-Nuclear reaction models and methods, *25.70.Pq*-Multifragment emission and correlations

I. Introduction

The understanding of mechanisms at play in ion collisions involving one projectile of high energy (typically several hundreds of MeV per nucleon) has been a long effort of nuclear science since the advent of GeV ion-beams, *e.g.* at the LBNL accelerator in the $70's$. These a priori complex processes were leading to rather simple patterns in the observables, such as the power laws found on the production cross sections as a function of the detected fragment charge [1]. In this landscape, spallation encompasses nuclear reactions induced by the collision of a particle, usually a hadron with a kinetic energy in the GeV range with a nucleus, or heavy-ion collisions where both nuclei are weakly excited [2]. Motivations for studying spallation mechanisms were also driven by potential applications of high-intensity GeV-proton beams impinging on high-Z targets for energy production, nuclear-waste transmutation or to build high-flux neutron-sources for other fields of science. One of the most interesting features of spallation is the production of large average numbers of neutrons per incident-hadron, which permits to design new neutron-sources like the European Spallation Source (ESS) [3] or the subcritical fast-neutron research reactor MYRRHA [4].

Spallation is usually modeled as a process in two steps correponding to different time scales in the reaction. On the shortest times, the physics is described by the intranuclear cascade, which consists in series of incoherent nucleon-nucleon collisions, which can transfer up to the total initial kinetic energy of the projectile to the target nucleus. The intranuclear cascade stops in the models when the energy transferred from the projectile is *uniformly distributed* among all the nucleons of the remaining nucleus. During this phase energetic particles may escape from the target nucleus. Throughout this paper, the excited nuclear system at the end of the cascade is called the prefragment.

The two-step picture relies on the hypothesis that the deexcitation mechanisms are collective processes occurring at the scale of the whole nucleus and hence, not influenced by the way the prefragment is produced. Therefore, this prefragment is only described by global variables such as its charge, mass, excitation energy and total angular momentum. The range of excitation energy which can be reached at the end of the cascade is broad enough to open different deexcitation channels like (light-) particle evaporation, heavier fragment production or fission. It is one of the aims of the present paper to test with observables the two-step hypothesis and measure the contributions of the different prefragment decay channels in the reactions $^{136}\mathrm{Xe} + \mathrm{p}$ and $^{136}\mathrm{Xe} + ^{12}\mathrm{C}$.

In our experiment we have used the inverse kinematics technique. At GeV-per-nucleon kinetic energies, it has the advantage of clearly separating in the detectors' frame the particles and fragments of small energy in the projectile rest-frame, *i.e.* essentially produced during the decay of the prefragment, from those of high kinetic energy, generated during the intranuclear cascade. The first type of particles are indeed efficiently boosted to forward angles, essentially at the velocity of the beam, whereas the particles of the second type have low energies in the lab frame and are widely spread around the beam axis. To take advantage of this efficient boost, two strategies were chosen in the literature: Either ensuring an accurate kinematics reconstruction of the deexcitation fragments close to the beam direction as was done at the fragment separator (FRS) of GSI (*e.g.* [5]), where the longitudinal (*i.e.* parallel to the beam axis) momentum distributions are measured for individual fragments identified both in charge and mass; or the detection of the many-fragment final states in coincidence on an event-by-event basis, as it was

*Article published in The European Physical Journal **A 55**, 11 (2019).

†ducret@ganil.fr

‡*Present address:* Facility for Rare Isotope Beams, Michigan State University, East Lansing, MI-48824 (USA)

§*Present address:* ANDRA, 1 Rue Jean Monnet, F-92290 Châtenay-Malabry, France

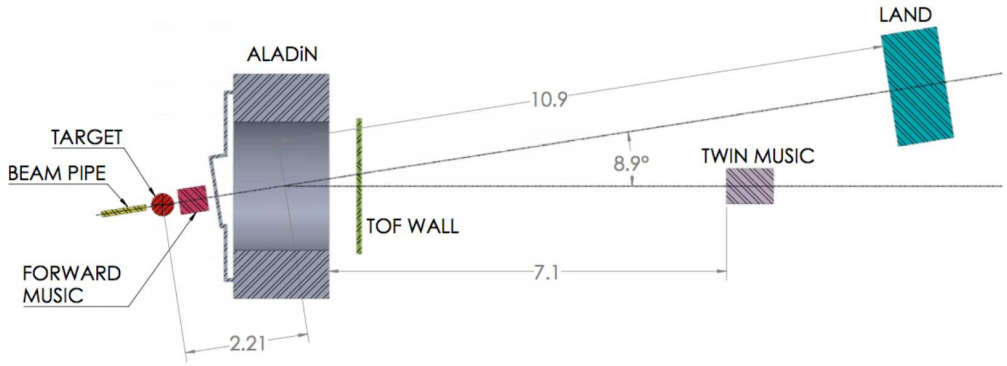

Figure 1: *SPALADiN experimental setup. The beam comes from the left. The target and an ionization chamber for the identification of the residue of the projectile (Forward MUSIC) are located upstream of the ALADiN magnet. The other detectors for charged fragments (ALADiN Tof-Wall and Twin MUSIC) and neutrons (LAND) are positioned downstream of the magnet.*

performed with the ALADiN setup [6, 7, 8] or at LBNL (see *e.g.* [1, 9]).

This paper is organised as follows. In section II, we describe the experimental setup as well as the data analysis principles. Section III is dedicated to the presentation of the element-production cross sections and the comparison with existing data for both reactions. In section IV, a comparison with models is performed. Section V is focused on the study of the prefragment-excitation-energy dependence of the reaction mechanisms.

II. The SPALADiN setup and data analysis

i. Setup

A sketch of the SPALADiN setup used for our experiment in April 2009 is shown in fig. 1. As compared with our previous experiment with this setup [8, 10], a different strategy with fast detectors and data acquisition is chosen, which permits higher counting rates. The ^{136}Xe beam at 1 GeV per nucleon is delivered from the SIS18 synchrotron with a charge state of 48. A thin plastic scintillator in front of the target fully ionises the beam ions to 54+, as recorded with the beam diagnostics in front of the target. The average energy loss in these diagnostics is of the order of a few MeV per nucleon. Two targets are employed: a cryogenic liquid hydrogen target (lH_2) [11], 80.53 mg/cm^2 thick, with ultrathin windows (6 ¯m aluminized mylar); a graphite foil (^{12}C, 386 mg/cm^2). In order to subtract the empty-target contribution to the different observables, data were taken with identical triggers and an empty target for lH_2 and without target for ^{12}C. To keep the dead-time of the data acquisition at a level or below 30%, the beam intensity was set at an average value of 3 10^3 ions/s.

The residue of the projectile is identified in a multiple- sampling ionization chamber (MUSIC), upstream of ALADiN, the "Forward MUSIC" (FM) [12], and a double-volume MUSIC, the "Twin MUSIC", downstream of ALADiN (TwM). FM is composed of four anodes. Its total efficiency (combined acceptance and detection efficiency) is close to 100% with a charge identification down to $Z = 12$ (fig. 2). TwM is made of two identical detection volumes, separated by a common central cathode. Eight triangular anodes collect the ionization signals and allow for the reconstruction of the track horizontal, transverse coordinates of the points sampled on the track, with the drift time providing the determination of their vertical coordinates [13]. Because of the angular dispersion of the fragments and of the settings of TwM's electron-

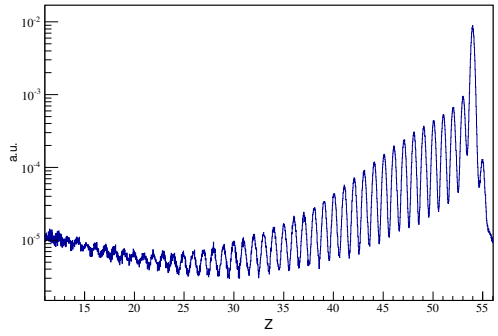

Figure 2: *Charge spectrum obtained in the Forward MUSIC (*lH_2 *target, no empty-target subtraction).*

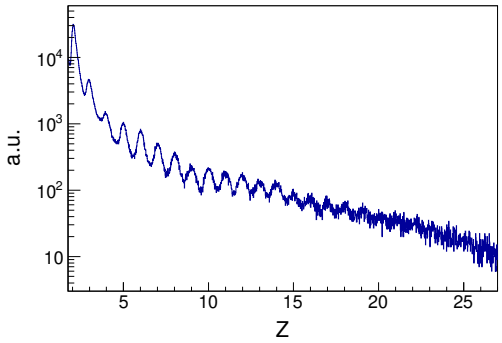

Figure 3: *Charge spectrum obtained in one scintillator of the* `TOF` *wall.*

ics, the geometrical losses in this detector are not negligible and strongly charge dependent: from around 75% for charge $Z = 12$ down to 20% for $Z = 40$ and 15% for the heaviest residues. Both ionization chambers are filled with P10 gas, a mixture of 90% Ar and 10% methane.

Thanks to the Lorentz boost provided by the inverse kinematics ($\gamma_{\text{Lorentz}} \simeq 2$ at 1 GeV), most of the lighter fragments ($Z \leq 12$) produced in the prefragment decay are detected in the ALADiN time-of-flight wall (`TOF`) [14, 15]. `TOF` is made of two layers of 96 plastic scintillators readout at both ends by photomultipliers. The scintillators are 10 mm thick, 1100 mm long and 25 mm wide. In order to avoid damages in the scintillator plastic caused by non-interacting beams of high Z, there is a hole in the middle of the five central scintillators in `TOF` corresponding to the passage of the beam. `TOF` ensures the charge identification up to approximately $Z = 23$ (fig. 3). Because of this hole, fragments of charge above $Z \sim 12$ in our experiment pass mostly through the hole and are identified in `TwM`. As seen in previous experiments, the smallest identified charge in `TOF` is $Z = 2$. After corrections obtained with a dedicated calibration of `TOF`, performed at the end of the experiment, the time resolution is 300 ps (RMS) for fragments of charge $Z \geq 4$ and ~ 550 ps for $Z = 2, 3$. The vertical position resolution is of the order of 5 cm. It is to be emphasized that the charge identification as shown in fig. 3 may be difficult above $Z = 23$. Anyway a detailed look at this histogram and in other `TOF` scintillators shows a possible Z identification following the $Z \propto \sqrt{S}$ rule, where S is the signal, properly calibrated. Moreover, since `TOF`'s detection efficiency is constant with Z, the cross-section measurement in this range is sensitive only to uncertainties in the limits of integration of the counting rates. Varying those around the chosen values doesn't change the statistics by more than 20%, *i.e.* within the error bars shown in fig. 8 and 9 of the element-production cross sections. The acceptance of each `TOF` plane of scintillators is 95%, as seen in our simulation (iii below). Since the particle selection in `TOF` requires the identification of the charge in both planes and taking into account the 5% dead zone between the scintillators in each plane, the probability for a charged fragment to be detected in `TOF` in our experiment is 81 ± 3%.

LAND is used to detect neutrons in our experiment. LAND is placed 10 m downstream of ALADiN's exit, on the beam axis in order to cover the 2π azimuth around it homogeneously. The event selection is described in [16]. The calibration of the signals' amplitude and time correlations is based on cosmic rays, measured in dedicated runs performed before, during and after the experiment. We

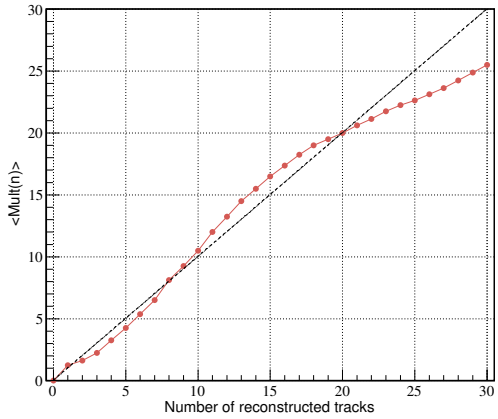

Figure 4: *Correlation between the number of reconstructed tracks and the mean number of neutrons in LAND* $\langle Mult(n)\rangle$.

employed the data analysis developed for preceding experiments [17, 18, 19].

The true number of neutrons emitted in each event cannot be reconstructed exactly from the LAND signal on an event-by-event basis because there isn't a one-to-one relationship between a LAND signal and a neutron impinging on this detector. Therefore, the data analysis reconstructs an *average* neutron multiplicity for each event, which corresponds to the mean value of the neutron multiplicity that can generate the number of neutron tracks reconstructed by the analysis (sets of coherent and independent time and amplitude signals). The LAND analysis is calibrated by mixing LAND signals from a deuteron break-up calibration experiment [16] and from events of our experiment which have the same characteristics as those of the deuteron break-up experiment. Both sets of events lead to the same calibration. In our experiment, the average neutron multiplicity is between 5 and 6, spanning a range from 1 (LAND is part of the data acquisition trigger) to 25. LAND efficiency to single neutrons is evaluated by two methods: 1) A one-parameter fit of multiplicity spectra from our simulation to the data; 2) The determination of the production cross section of Cs ($Z = 55$) in the reaction ^{136}Xe + p requiring no detected neutrons (the data acquisition is triggered only on incoming-beam particles) and comparing the results to existing data from FRS of fully identified Cs isotopes [13, 20]. Both methods lead to a LAND efficiency of 80% $\pm$ 3% for single neutrons. This is significantly higher than in our previous experiment [8] for two reasons: 1) The number of working scintillators in LAND is larger in this experiment than in the previous one; 2) In this previous experiment, LAND, which was installed much closer to the ALADiN magnet exit, was not centred on the beam direction but transversely shifted (towards higher magnetic rigidities) in order to avoid charged fragments not sufficiently bent by ALADiN, hence reducing LAND geometrical acceptance.

ii. Data analysis

The first task of the event selection is to ensure that the data are not degraded by secondary reactions of the fragments along their paths through the setup. The essential condition for this is the requirement that the charge of the projectile residue (the largest charge in the event) is the same in `FM` behind the target and either in `TwM` or in `TOF` downstream of ALADiN. The proportion of selected events is given in fig. 5 and varies from 40% for $Z = 12$ to 70% for $Z = 55$. In order to compensate for these losses a weight is given to each event. The total weight W of an event is defined as the product over all detected charged fragment/particle of individual weights $w(i)$ in the event. Let N_Z be the number of charged particles in the event, including the projectile residue. We have:

$$W = \prod_{i=1}^{N_Z} w(i) \qquad (1)$$

This approach permits to take into account the losses encountered by large-multiplicity events relatively to lower-multiplicity ones. This total weight is used for observables involving all the detected charged fragments. For more inclusive observables like

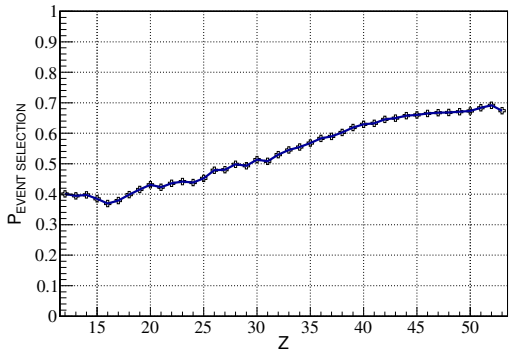

Figure 5: *Fraction of events with the same highest charge Z determined in* `FM` *and either in* `TOF` *or* `TwM`.

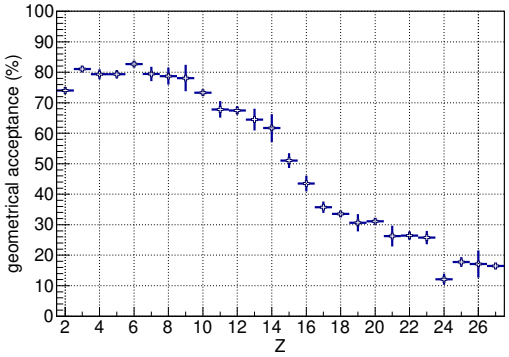

Figure 6: *Acceptance in the ToF wall as a function of the charge Z, obtained in the GEANT4 simulation (*`INCL++` *with* `ABLA07`, ^{136}Xe + p*).*

the fragment production cross sections, partial weights are computed. $\forall i$, $w(i)$ is computed from a "survival" probability as $\forall i$, $w(i) = P^{-1}_{\text{survival}}(i)$, with $P_{\text{survival}}(i) = 1 - P_{\text{reaction}}(i)$, where $P_{\text{reaction}}(i)$ is the probability for the charged fragment i to undergo a charge changing reaction in the setup. For the projectile residues, whose charge is measured in `FM`, $P_{\text{reaction}}(i)$ is determined from the data. For the lighter ions, $P_{\text{reaction}}(i)$ is computed from the inelastic cross sections parametrized by J. Jaros *et al.* [22]. We underline that this method is not applied to neutrons, whose absorption is computed directly in our simulation based on an estimate of $P_{\text{reaction}}(\text{n})$ by Tripathi *et al.* [23]: $P_{\text{reaction}}(\text{n}) \simeq 1.4\%$.

iii. GEANT4 simulation

The simulation of the experiment is performed within the GEANT4 environment [24, 25]. We have used different versions of GEANT4 throughout the duration of this work, from 4.8.1 for the simulation of our setup prior to the beam time to 4.10.4 for the calculations we are still performing, without noticeable differences in our results. The particle transport is fed with spallation events produced by standalone versions of collision models coupled with deexcitation codes. We do calculations for both reactions of the present work. We use two collision models: the intranuclear cascade `INCL++` [26, 27, 28, 29, 30, 31, 32] and the fast collision and excitation model `ABRA` [33, 34, 35, 36] and three deexcitation codes: `ABLA07` [37], `GEMINI++` [39, 40] and `SMM` [41]. The geometry of our setup is included in details. The charged-particle tracking in the ALADiN magnetic field is performed in a 3D map. The aim of the simulation is twofold. First it is used as an experimental filter in order to compare the models' predictions to the data, once the detection efficiencies are taken into account. Second, for the lighter ions essentially detected in `TOF`, we rely on the simulation to estimate the acceptance of the setup, in particular to compute the probabilty for every ion species to go through the active volume of the `TOF` scintillators. With `INCL++` the results are almost independent of the deexcitation models coupled to it. Hence the acceptances we use for our data analysis are averaged over these three models and are shown in fig. 6. We compare the setup acceptance calculations done with `INCL++` and `ABRA` linked to `ABLA07` in fig. 7 for the reaction ^{136}Xe +^{12} C. We choose to show this reaction only for the sake of simplicity, the results are the same for ^{136}Xe + p. For each ion species, identified with its charge, the acceptance is computed as the ratio between the number of particles passing through the corresponding detector (either `TOF` or `FM` or `TwM` or LAND) and the num-

ber of particles produced by the event generator. We observe comparable behaviours with Z, and values close to unity above Z=12, with INCL or ABRA, even though their predictions for the kinetic-energy spectra of the fragments produced in the reaction are very different in the ^{136}Xe rest frame, ABRA's spectra being broader than INCL's ones. As discussed in [29] by D. Mancusi *et al.*, INCL, linked to ABLA07 or SMM or GEMINIXX, is unable to reproduce the longitudinal-velocity ($v_{||}$) distributions of the fragments, identified in mass and charge, which were measured at GSI-FRS by P. Napolitani *et al.* [21]. Such a discrepancy between the model we employ in the present work and measured data raises the question of the sensitivity of our simulation to the fragment kinematics in the ^{136}Xe rest frame. Indeed, this sensitivity is negligible. This statement is based on the characteristics of the ALADiN magnet (bending power and physical length), equipped with a large entrance aperture as well as a large exit window, which is almost fully covered by TOF. This full coverage ensures an efficient detection over a large range of magnetic rigidity around the beam's value. TwM, further away behind ALADiN's exit provides an additional identification of the fragments, essentially close the beam trajectory. This permits a complete coverage of the fragment velocity spectra in the ^{136}Xe rest frame, as measured at GSI-FRS or as computed by the models, independently of their shapes, Fig. 7 illustrates this, where the acceptance of the setup, computed for the reaction ^{136}Xe +^{12} C, is very close to unity. Furthermore, as was discussed in [13], the detected-fragment position distributions on TOF computed with our simulation compares successfully in width and shape with the data, for each reaction product identified with its charge.

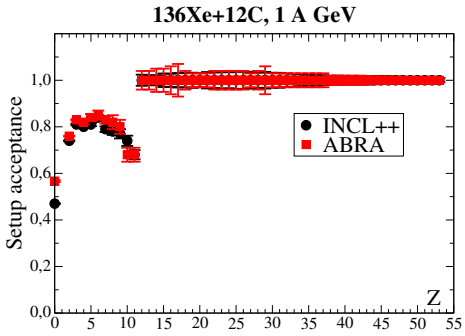

Figure 7: *Geometrical acceptance of the setup, as a function of the ion charge, as computed with GEANT4 using* ABRABLA *and* INCL++ *(with* ABLA07*) for the reaction* ^{136}Xe +^{12} C. *The bin* $Z = 1$ *is not shown because these particles are not detected in the experiment.*

III. Element-production cross sections

The element production cross sections of our experiment are shown in figs. 8 and 9 for ^{136}Xe + p and ^{136}Xe +^{12} C respectively. The SPALADiN cross sections are composed of two sets of data. For the smaller charges the values are obtained from TOF after detection-efficiency and acceptance corrections. For the larger charges, FM is used to extract the element cross sections. It should be pointed out that both sets of data provide two independent determinations of these cross sections and that they nicely agree in the Z-range of overlap. Our data points exhibit the well-known U-shape, with a dip level around 0.2 mb for the fragments of charge $Z \in [10, 25]$ for ^{136}Xe + p and $\sim$ 20 mb for the ions of charge $Z \in [12, 40]$ for ^{136}Xe +^{12} C.

The comparison with the GSI-FRS data of Napolitani *et al.* [20] for the ^{136}Xe + p reaction puts in evidence three regions in the Z domain: 1) A very good agreement between both data sets at larger Z, down to $Z \simeq 30$; A fair agreement below $Z = 6$; A systematic discrepancy between the two experiments on the plateau level from $Z = 8$ to $Z = 26$, the FRS data being systematically above and incompatible with ours given the error bars of both experiments. Attempting to explain this disagreement seems a difficult task. The fair agreement between both experiments below $Z = 6$, *i.e.* where the acceptance corrections necessary to obtain the element-production cross sections in the FRS data anal-

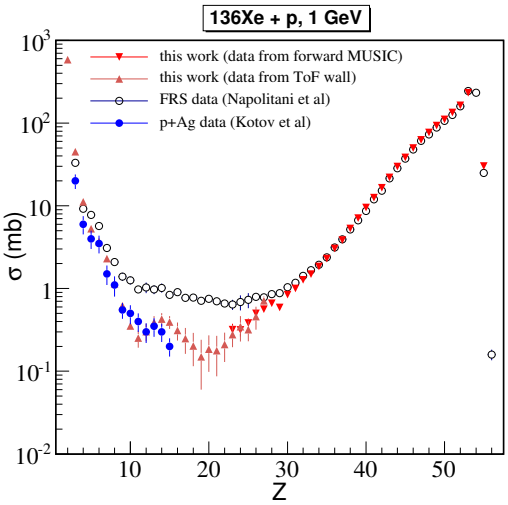

Figure 8: *Element production cross sections for* ^{136}Xe + p *(1 GeV per nucleon). SPALADiN data are shown in red (see text for details) and compared to FRS data by Napolitani* et al. *[20] and Kotov* et al. *[42].*

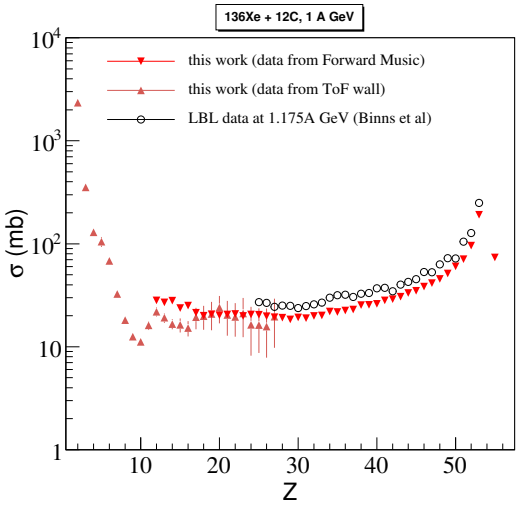

Figure 9: *Element production cross sections for* ^{136}Xe +^{12} C *(1 GeV per nucleon). SPALADiN data are shown in red (see text for details) and compared to LBNL data by W. R. Binns et al. at 1.175A GeV [9] in black.*

ysis are the largest [20] indicates that those are well in hand. Moreover, the good agreement with the data of Kotov *et al.* [42] on a system close to ours (p +$^{\text{nat}}$ Ag, at 1 GeV proton beam energy) measured by a different method and in direct kinematics underlines the good agreement between FRS data and our experiment. Above $Z = 6$ however, even if our data remain clearly compatible with Kotov's work, they diverge with FRS as Z increases towards a range where the acceptance and detection efficiency vary smoothly and slowly in both experiments. For $Z \geq 23$, we see a good agreement between our two determinations of the cross-sections, *i.e.* with `FM` alone or with `TOF`. This gives confidence in our efficiency and acceptance estimates since: 1) There is basically 100% acceptance and detection efficiency in `FM` as mentioned above for these elements, `FM` can therefore be considered as a detection reference in our experiment; 2) `TOF` acceptance in this range is rather small since most of these projectile residues pass through the hole of `TOF`, hence acceptance corrections are the largest in this Z range. This agreement between `TOF` and `FM` emphasizes the quality of these corrections. Furthermore the very good agreement between both data sets for $Z \geq 27$ shows controlled efficiencies and empty-target-contribution subtraction in both experiments.

All in all, no obvious explanation can be found for the observed partial disagreement between the GSI-FRS data and ours. We believe that this discrepancy should be the ground for a third experiment, preferably with a large acceptance detection setup, in order to remain independent from large acceptance-corrections.

Our element-production cross sections for the reaction ^{136}Xe +^{12} C in fig. 9 exhibit also a good coherence between the `FM`'s determination and the `TOF`'s down to $Z = 12$. We have compared our data with the LNBL experiment of Binns *et al.* [9]. We notice in this figure a systematic and constant 30% difference between the two sets of cross sections, ours being below Binns'. This normalisation difference can't be explained by the difference of beam energy of the two experiments, the energy dependence of the cross sections being very slow around 1 GeV. This 30% difference is large as compared

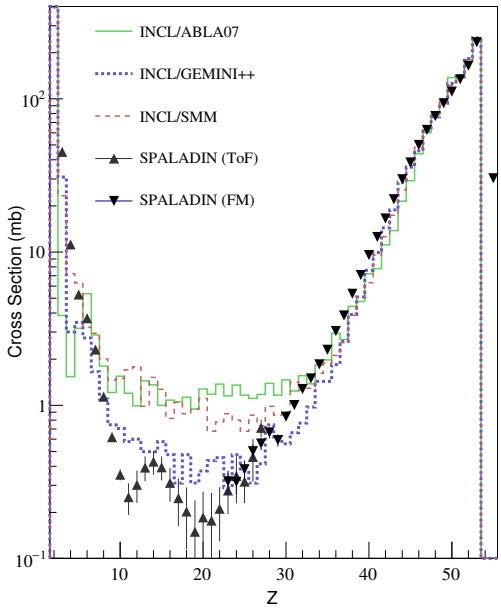

Figure 10: *Element production cross sections of the* ^{136}Xe + p *reaction (black symbols), compared with models:* `INCL++` + `ABLA07` *(solid green) /* `GEMINI++` *(dotted blue) /* `SMM` *(dashed red).*

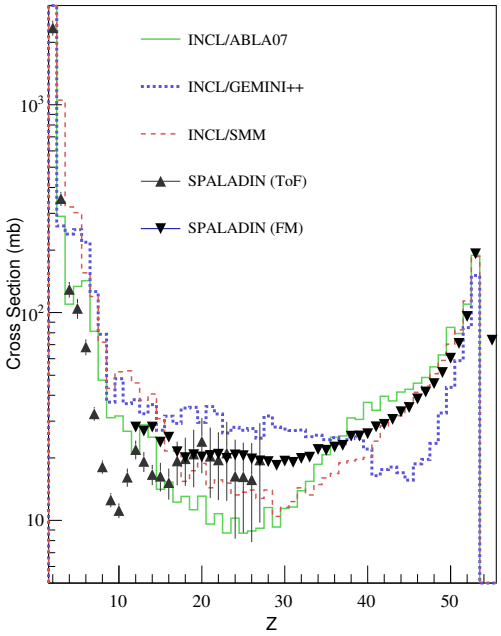

Figure 11: *Element production cross sections of the* ^{136}Xe +^{12} C *reaction (black symbols), compared with models:* `INCL` + `ABLA07` *(solid green) /* `GEMINI++` *(dotted blue) /* `SMM` *(dashed red).*

with the various corrections done in the data analyses of both experiments (see [9] for the detail of their analysis). Hence an explanation is here also difficult to find. A possibility may be found in the detection and data-acquisition efficiencies of Binns' experiment. These efficiencies are correctly controlled in our experiment as discussed above for ^{136}Xe + p compared with other data sets. Another possibility may come from the "thick-target" corrections performed in [9], where their ^{12}C target was more than a factor 3 thicker than in the present experiment.

IV. Comparison with models

As mentioned above, we compare our data with models coupling an intranuclear cascade and a statistical deexcitation in the two-step hypothesis. These models are used as event generators of the setup GEANT4 simulation, for the comparison with our data. The simulated and experimental observables are normalized to absolute cross sections. We used only one cascade, `INCL++`, coupled with three deexcitation codes for the comparison with the data.

The Liège intranuclear cascade (`INCL++` version in the present work, from here on referred to as `INCL`, in order to simplify the notations is being developed for almost 40 years [26, 27, 28, 29, 30, 31, 32] for the description of nucleon-, pion-, light-ion-induced collisions in the 150-3000 MeV incident energy range. We wish to emphasize two features of `INCL`. The first one, as noted by D. Mancusi *et al.* [32], is that `INCL++` is equivalent to `INCL4.6` as far as the physics it is modelling is concerned for the proton - nucleus reactions. In partic-

ular, its predictions are very close to those of INCL4.6. The second feature is the ability of INCL to compute reactions with light ions (up to $A = 18$) as projectiles on target nucleus. This was initiated for INCL4.6 [30] in a mathematically coherent way and has been extended in INCL++ [32]. INCL describes a light-ion projectile as a set of nucleons, off-shell in the reaction initial state in order to take into account the nuclear binding energy of the ion. Each nucleon has a Fermi momentum in the light-ion rest frame and an initial position, randomly chosen. The interaction is treated on the basis of the Coulomb trajectory towards the target nucleus of the light-ion projectile and for each nucleon of the projectile whose own trajectory makes it encounter a collision with a nucleon of the target nucleus, the scattering and collision calculation is performed. The deexcitation models combined with INCL are ABLA07, SMM and GEMINI++. ABLA07 [37] describes the deexcitation of the prefragment (*i.e.* the end nuclear state of the cascade) via evaporation of fragments and light particles and fission. ABLA07 contains a multifragmentation module, which is triggered if the excitation energy of the prefragment exceeds a threshold. This threshold can be chosen constant (default option of the model) at $E^\star/A = 4.2$ MeV, or can be set dependent on the mass of the excited nuclear system (the prefragment, in the two-step picture), following the systematics of J.B. Natowitz *et al.* [38], cited in [37]. In the mass range of the prefragments produced in ^{136}Xe + p and ^{136}Xe +^{12} C, the mass dependence leads to threshold values of the excitation energy per nucleon close to 4.2 MeV. Lines corresponding to this value are drawn in figs. 14 and 15 below, which show that the reaction on the proton remains essentially below it, whereas a sizeable part of the statistics recorded for ^{136}Xe +^{12} C is above it. The production of intermediate-mass fragments (IMF) is performed within two approaches: Either in the generalized Weisskopf-Ewing formalism [43] or with the emission of light clusters during the breakup of the excited prefragment. This last channel is opened when the excitation energy per nucleon of the prefragment is above a specific freeze-out value [37]. Above the Businaro-Gallone point, competition with fission is included, but of marginal interest in our work. GEMINI++, developed by R. J. Charity *et al.* [39, 40] describes the prefragment deexcitation as a series of binary decays. The emission of light particles ($Z \leq 3$ by default) follows the Hauser-Feshbach evaporation formalism [44]. The conditional saddle-point formalism of Moretto [45] with the Sierk's finite-range barriers [46] is used for heavier fragments ($Z \geq 4$). Fission widths of heavy nuclei are computed in a refined version of Bohr-Wheeler's model [47]. The combinations of INCL with ABLA07, GEMINI++ and SMM were recognized among the best performing models at the IEAE workshop held in Trieste in 2008 on the benchmarking of spallation models [48, 49, 50].

i. Element-production cross section

Figs. 10 and 11 show the comparison with the data of the three models described above, for both reactions respectively. For the first one the models reproduce well the production cross-sections close to the initial nucleus down to $Z \in [\sim 30, 34]$, where the predictions start to diverge. INCL + ABLA07 remains in good agreement with our data in this range but, below $Z = 30$ it stays in close to the GSI-FRS data, as was observed by J. Alcántara-Núñez *et al.* in [51], in their study of the reaction ^{136}Xe + d at 500 MeV per nucleon, where they compare their data with measurements on ^{136}Xe + p at 1000 and 200 MeV per nucleon[1]. In the range $Z \in [28, 34]$, our data are better described by INCL + SMM but below this range INCL + GEMINIXX is closer to our data. This is coherent with the work of Kotov *et al.*, whose data, close to ours in the range $Z \in [3, 14]$ are better reproduced by this model. For ^{136}Xe +^{12} C, the comparison with the models exhibit large discrepancies.

[1] Note that in [51] INCL4.6 is used instead of INCL++ but as mentioned above in the present work, both versions are equivalent.

Type	Residue	neutrons	He	fragments
(1)	1	≥ 1	0	0
(2)	1	≥ 1	≥ 1	0
(3)	1	≥ 1	0	≥ 1
(4)	1	≥ 1	≥ 1	1
(5)	1	≥ 1	≥ 0	≥ 2

Table 1: *Definition of the different types of final states used in the decomposition of $\sigma(Z_{\text{bound}})$ according to the number of detected He nuclei and fragments ($Z \geq 3$).*

The Z dependence of the cross section is well predicted by `INCL + SMM` above $Z = 40$ and extremely poorly by `INCL + GEMINIXX`. Below this charge the models diverge to large extents and none reproduces the Z dependence measured in our experiment.

ii. Final-state decomposition

In order to study the content in particles and fragments of the final states of both reactions, which helps in assessing the relative importance of the different deexcitation mechanisms, we define the total detected charge for each event as:

$$Z_{\text{bound}} = \sum_{Z_i \geq 2} Z_i \qquad (2)$$

where the sum runs over all detected particles or fragments in the event. As discussed below and as was shown by the ALADiN group [6], Z_{bound} is correlated with the average excitation energy per nucleon of the prefragment at the end of the intranuclear cascade. We determine $\sigma(Z_{\text{bound}})$, which we decompose into contributions from different final-state contents corresponding to different prefragment deexcitation channels, as was done *e.g.* for the ^{56}Fe + p by Le Gentil *et al.* [8], according to the number of He nuclei and fragments ($Z \geq 3$), as specified in table 1.

Figs. 12 and 13 show the decompositions of $\sigma(Z_{\text{bound}})$ for ^{136}Xe + p and ^{136}Xe +^{12} C respectively, as measured in our experiment

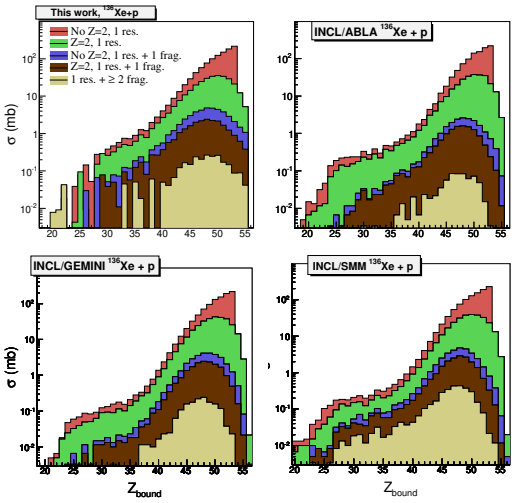

Figure 12: *Contributions to $\sigma(Z_{\text{bound}})$ of the final states of the reaction in five types according to their content in fragments ($Z \geq 3$) and helium nuclei as defined in table 1 for ^{136}Xe + p.*

(upper-left in both) and as computed by the models. We see that type (1) final-state distribution dominates at large Z_{bound} (most peripheral collisions). For ^{136}Xe + p we observe that the partial cross sections of types (2) to (5) have a maximum around $Z_{\text{bound}} = 48$, type (2) dominating the other three down to the smallest values of Z_{bound} where we can extract a cross section from the data. This feature points clearly to the fact that for this reaction the production of fragments remains mostly a rather low prefragment-excitation-energy mechanism and that over the whole prefragment distribution covered in our experiment, evaporation, either of neutrons and/or of He nuclei is dominating. For ^{136}Xe +^{12} C (fig. 13), type (1) dominates the other final states down to $Z_{\text{bound}} \simeq 40$, below which value type (2) is the most contributing type of final states, down to the lower Z_{bound}. Contrary to the other channels, the partial cross section $\sigma(Z_{\text{bound}})$ of type (2) final states is constant over the range $Z_{\text{bound}} \in [23, 48]$, at a value of ∼20 mb. The fragment production (types (3) to (5)) starts to contribute

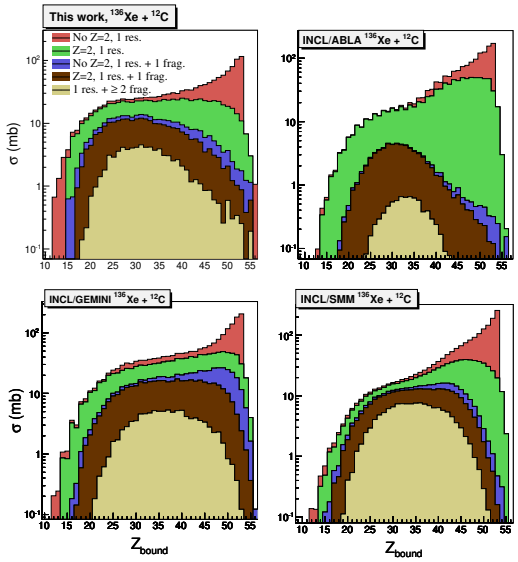

Figure 13: *Contributions to $\sigma(Z_{\mathrm{bound}})$ of the final states of the reaction in five types according to their content in fragments ($Z \geq 3$) and helium nuclei as defined in table 1 for ^{136}Xe +^{12} C.*

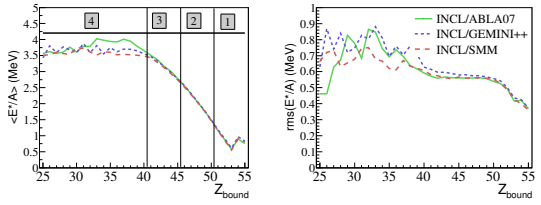

Figure 14: ^{136}Xe + p*: Correlation between the excitation energy per nucleon of the prefragment $E^\star/A$ and the detected charge of the events Z_{bound}, mean $\langle E^\star/A\rangle$ and rms, $\sigma\left(E^\star/A\right)$. $\langle E^\star/A\rangle$ and $\sigma\left(E^\star/A\right)$ values corresponding to each interval are given in table 2. The line at $E^\star/A = 4.2$ MeV is a threshold value in* ABLA07 *for the excitation energy of the prefragment above which the decay can be computed with a dedicated multifragmentation module.*

significantly below $Z_{\mathrm{bound}} = 50$, at variance with ^{136}Xe + p. Moreover it extends down to $Z_{\mathrm{bound}} \simeq 18$, as compared to a lower limit of $Z_{\mathrm{bound}} \simeq 30$ in fig. 12. We infer from these observations that the fragment production in ^{136}Xe +^{12} C is occurring on average for significantly higher excitation than in ^{136}Xe + p.

The three models reproduce only qualitatively the contributions of the different types of final states to $\sigma(Z_{\mathrm{bound}})$ for the bulk part of the cross section. For ^{136}Xe +^{12} C the proposed final state decomposition emphasizes the poor ability of the models to describe the most peripheral collisions, as noted above but emphasizing on the light-particle evaporation. This goes noticeably at variance with what can be seen for the reaction on the proton. The models predict the gross features of $\sigma(Z_{\mathrm{bound}})(\mathrm{type}(3,4,5))$: A maximum around $Z_{\mathrm{bound}} = 30$ with widths similar to our data. However, the Z_{bound} dependence is not well reproduced by the models, in particular for $Z_{\mathrm{bound}} \geq 40$, contrary to ^{136}Xe + p. This should be investigated in detail in the models.

V. Excitation energy dependence of the reaction mechanisms

As shown in the previous section, the decomposition of the final states as a function of Z_{bound} seems to point to a dependence of the mechanisms on the excitation energy at the end of the intranuclear cascade. Figs. 14 and 15 show the correlation between the excitation energy per nucleon $E^\star/A$ of the prefragment and Z_{bound} for ^{136}Xe + p and ^{136}Xe +^{12} C respectively, computed with the GEANT4 simulation of our setup. It must be underlined that the dispersion in the model predictions, for the average value $\langle E^\star/A\rangle$ as well as for the RMS, $\sigma\left(E^\star/A\right)$ is small, except for the highest $E^\star/A$ of ^{136}Xe +^{12} C. This small dispersion ensures a correlation independent of the de-excitation model. Based on this, we choose Z_{bound}, which is an observable, as a measure of $\langle E^\star/A\rangle$ to study the reaction mechanisms. As discussed in [13], Z_{bound} is preferred to the total multiplicity (TM) in the event, which has also been used in heavy-ion collision studies [53, 54, 55]. The reason relies essentially on the fact that, for given bins of TM, the distributions in $E^\star/A$ are not symmetric, with signifi-

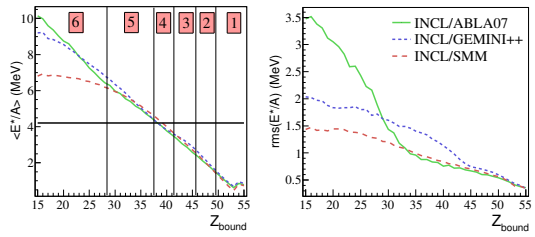

Figure 15: ^{136}Xe $+^{12}$C*: Correlation between excitation energy per nucleon of the prefragment $E^\star/A$ and the detected charge of the events Z_{bound}, mean, $\langle E^\star/A\rangle$ and rms, $\sigma(E^\star/A)$. $\langle E^\star/A\rangle$ and $\sigma(E^\star/A)$ values corresponding to each interval are given in tables 2 and 3.The line at $E^\star/A = 4.2$ MeV is a threshold value in* ABLA07 *for the excitation energy of the prefragment above which the decay can be computed with a dedicated multifragmentation module.*

	INCL / ABLA07	$\langle E^\star/A\rangle$ (MeV)	$\sigma(E^\star/A)$ (MeV)
1	$51 \leq Z_{\text{bound}} \leq 55$	0.835	0.525
2	$46 \leq Z_{\text{bound}} \leq 50$	1.850	0.655
3	$41 \leq Z_{\text{bound}} \leq 45$	2.990	0.605
4	$Z_{\text{bound}} \leq 40$	3.800	0.670

Table 2: *Mean excitation energy per nucleon for* Z_{bound} *intervals defined in fig. 14 for* ^{136}Xe + p.

cant differences between the average of the distribution $\langle E^\star/A\rangle$ and the most probable value $(E^\star/A)_0$, whereas Z_{bound} selections produce symmetric $E^\star/A$ distributions, peaked very close to $\langle E^\star/A\rangle$. Such differences may bias the interpretation of the results, therefore TM is not chosen.

In order to study the $\langle E^\star/A\rangle$ dependence of the reaction mechanisms, we have defined Z_{bound} / $\langle E^\star/A\rangle$ intervals numbered from [1] to [4] for ^{136}Xe + p (table 2) and [1] to [6] for ^{136}Xe $+^{12}$C (table 3), this second reaction covering a significantly broader spectrum than the proton reaction. This definition permits to have sufficient statistics in all the intervals.

	INCL / SMM	$\langle E^\star/A\rangle$ (MeV)	$\sigma(E^\star/A)$ (MeV)
1	$50 \leq Z_{\text{bound}} \leq 55$	0.790	0.560
2	$46 \leq Z_{\text{bound}} \leq 49$	1.980	0.710
3	$42 \leq Z_{\text{bound}} \leq 45$	3.080	0.800
4	$38 \leq Z_{\text{bound}} \leq 41$	4.095	0.890
5	$29 \leq Z_{\text{bound}} \leq 37$	5.400	1.15
6	$Z_{\text{bound}} \leq 28$	6.520	1.375

Table 3: *Mean excitation energy per nucleon for* Z_{bound} *intervals defined in fig. 15 for* ^{136}Xe $+^{12}$C.

i. Total multiplicity

Fig. 16 exhibits the evolution of the total multiplicity (TM) cross sections for the Z_{bound} bins defined in table 2 for ^{136}Xe + p (blue squares) and in table 3 ^{136}Xe $+^{12}$C (red crosses). In order to compare the reactions, we scale ^{136}Xe + p data points to those of ^{136}Xe $+^{12}$C according to:

$$\sigma_{\text{p,sc.}}(\text{TM}) \quad = \quad \sigma_{\text{p}}(\text{TM}).\frac{\sigma_{^{12}\text{C}}\big(\langle E^\star/A\rangle\big)}{\sigma_{\text{p}}\big(\langle E^\star/A\rangle\big)} \quad (3)$$

where $\sigma_{\text{p}}(\text{TM})$ is the cross section corresponding to the total multiplicity TM, integrated in the selected $\langle E^\star/A\rangle$ bin, $\sigma_{^{12}\text{C}}\big(\langle E^\star/A\rangle\big)$ is the cross section integrated in the $\langle E^\star/A\rangle$ bin over all TM values for ^{136}Xe $+^{12}$C and, the corresponding integrated cross section for ^{136}Xe + p being $\sigma_{\text{p}}\big(\langle E^\star/A\rangle\big)$. The striking feature of fig. 16 is that both data sets almost overlap in the four common intervals in $\langle E^\star/A\rangle$, with evolutions of shapes very similar as $\langle E^*/A\rangle$ increases. Such an evolution of TM as a function of $\langle E^\star/A\rangle$ is not trivial since it takes into account the multiplicity of detected neutrons which doesn't contribute to Z_{bound} (which sets $\langle E^\star/A\rangle$). In fig. 16, we notice the independence of TM on the entrance channel (*i.e.* the reactions) leading to a given average excitation energy per nucleon of the prefragment. This is a strong support on the two-step model hypothesis used throughout this paper.

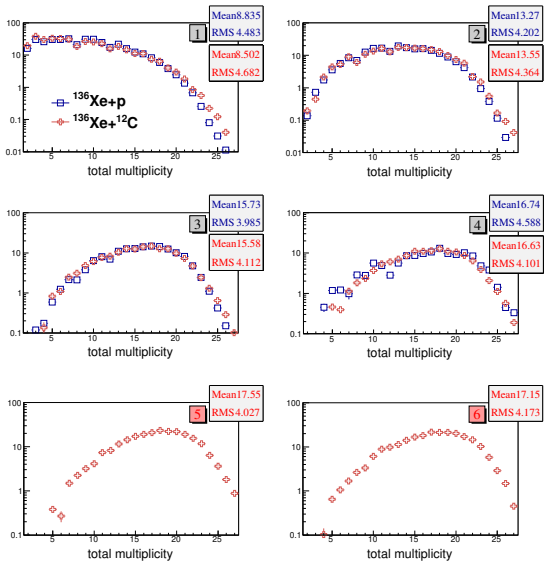

Figure 16: *Evolution of the total detected multiplicity as a function of* $\langle E^\star/A\rangle$ *for* ^{136}Xe + p *(blue squares) for* ^{136}Xe +^{12} C *(red crosses). Values for* $\langle E^\star/A\rangle$ *are defined in tables 2 and 3. The* ^{136}Xe + p *data are scaled to the* ^{136}Xe +^{12} C *data (see text).*

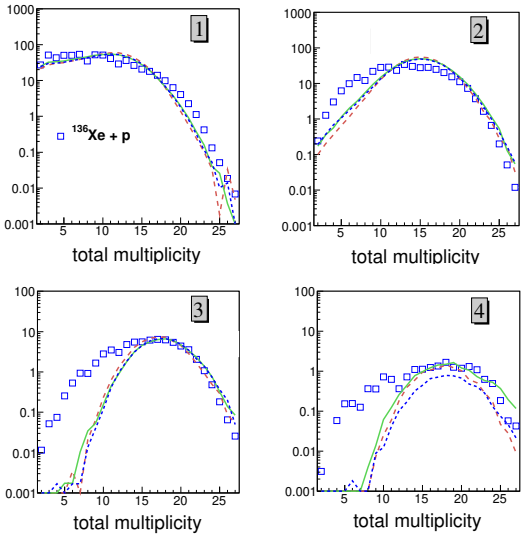

Figure 17: *Evolution of the total-multiplicity (TM) distributions with* $\langle E^\star/A\rangle$ *for* ^{136}Xe + p *(blue squares) compared with the deexcitation models:* `ABLA07` *(solid green),* `GEMINI++` *(dotted blue) and* `SMM` *(dashed red) coupled with* `INCL`.

The comparison of the models with the (unscaled) data is presented in figs. 17 and 18 for ^{136}Xe + p and ^{136}Xe +^{12} C respectively. The models reproduce reasonably well the evolution of the TM distributions with $\langle E^\star/A\rangle$ for both reactions with the caveat of the low-TM side of the distributions (TM $\leq$ 12) for ^{136}Xe + p, for which the data points are largely underestimated by the models for the three highest $\langle E^\star/A\rangle$ bins with a difference becoming larger as $\langle E^\star/A\rangle$ increases. Such a discrepancy is not observed for ^{136}Xe +^{12} C, for which we see a fair agreement between our data points and both `ABLA07` and `GEMINI++`, coupled with `INCL`. This scaling is indeed reproduced by `SMM` at the price of a strong disagreement with the data for both reactions on the low-TM side of the distributions.

As underlined above, the TM distributions scale very well in the selected bins of $\langle E^\star/A\rangle$. We see in figs. 17 and 18 that this is not the case for the models' predictions, whose distribution-shapes change from one reaction to the other in their low-TM side. The agreement between the models and the data on the positions of the maxima of these distributions as well as on the shapes of the high-TM side of the distributions drives to the conclusion that the models are to a major extent correct in describing this observable, where evaporation of light particles dominates the deexcitation channels. We have performed different model calculations in the scope of this data analysis, where we have tested the sensitivity of the TM distributions to the different variables characterizing the prefragment at the end of the cascade: its mass, charge, excitation energy and total angular momentum as was done in [56] to study the fission channels of spallation on heavy nuclei. For this study, we have changed the prefragment mass and charge distributions at the end of the cascade phase of ^{136}Xe + p to resemble that of ^{136}Xe +^{12} C. During the cascade phase the ^{136}Xe nucleus loses notably more nucleons in the reaction ^{136}Xe +^{12} C than in the reaction

^{136}Xe + p, with therefore broader mass and charge distributions of the prefragment, for a given $E^\star/A$ bin (see fig. 19). We have also changed the total angular momentum distribution of the prefragment at the end of the cascade for ^{136}Xe +^{12} C to resemble that of ^{136}Xe + p. We could observe a very low sensitivity of the predictions to the angular momentum of the prefragment, for all the deexcitation models. Shifting the excitation energy distributions only changed the position of the maxima of the TM distributions in the Z_{bound} bins but not their widths, hence not improving the agreement between models and data for low-TM cross sections. We found that in given $\langle E^\star/A\rangle$ bins, shifting the mass and charge distributions of the prefragments arising from the intranuclear cascade of the reaction ^{136}Xe + p towards smaller values helps much in filling the gap between our data and the models. We conclude that the events with final states characterized by low TM are related to prefragments with charge and mass smaller than the average values corresponding to $\langle E^\star/A\rangle$ (the mass and the charge of the prefragment are correlated with $E^\star/A$ at the end of the cascade, as shown in fig. 19). Therefore, the difference we observe on the low-TM side distributions can be interpreted as an insufficient mass and charge loss *during the cascade phase*, as a function of $E^\star/A$, in INCL for the ^{136}Xe + p reaction. In this respect, INCL computes mass and charge prefragment spectra, which permit to fit well the data for ^{136}Xe +^{12} C during the deexcitation.

ii. Fragment production

To investigate further the $E^\star/A$ dependence of both reactions, we study the evolution of the content of their final states, zooming on the number of fragments ($Z \geq 3$, including the projectile residue mentioned in table 1). The data points of this observable are shown in fig. 20 for both reactions. Data are presented as:

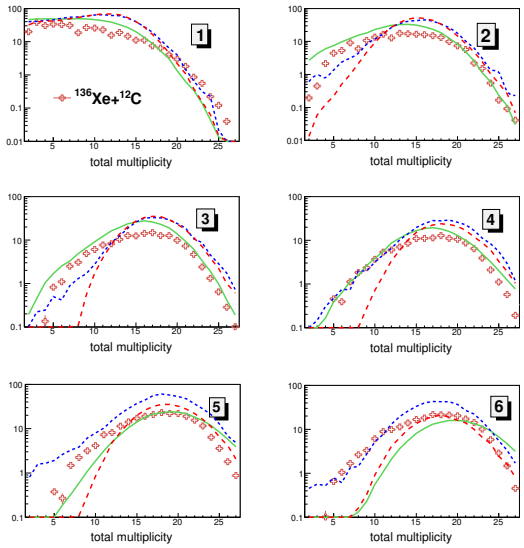

Figure 18: *Evolution of the total-multiplicity (TM) distributions with $\langle E^\star/A\rangle$ for ^{136}Xe +^{12} C (red crosses) compared with the deexcitation models:* ABLA07 *(solid green),* GEMINI++ *(dotted blue) and* SMM *(dashed red) coupled with* INCL.

$$R_{\text{FS}} = \frac{\sigma_{\text{FS}}\big(\langle E^\star/A\rangle\big)}{\sigma\big(\langle E^\star/A\rangle\big)} \tag{4}$$

where $\sigma\big(\langle E^\star/A\rangle\big)$ is the cross section integrated over all types of final states (FS) and on the Z_{bound} interval corresponding to $\langle E^\star/A\rangle$ according to tables 2 and 3; in this definition, $\sigma_{\text{FS}}\big(\langle E^\star/A\rangle\big)$ is the cross section integrated over the same Z_{bound} interval but for the selected final-state content FS. Three types of final states are selected: one-fragment (FS=1, circles), two-fragment (FS=2, squares) and 3 or more (FS $\geq$ 3, triangles). We see in fig. 20 that in both reactions, and as was noted in section ii, the final states FS = 1 fragment dominate the cross section up to the highest $\langle E^\star/A\rangle$ bin reached with ^{136}Xe + p. For the higher $\langle E^\star/A\rangle$ points, the contribution of these final states decreases further down to $R_{\text{FS=1}} \simeq R_{\text{FS=2}}$. As for the total multiplicity (TM) distributions, we also see in this figure that the data points of the two reactions almost overlap for FS = 1 or 2 fragment(s), underlining the

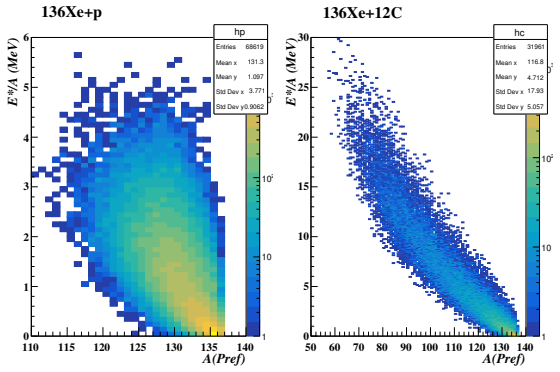

Figure 19: *$E^\star/A$ - prefragment-mass distributions computed with* INCL *for the ^{136}Xe + p reaction (left) and for ^{136}Xe +^{12} C (right).*

two-step scenario for the reaction description, with a selection of the prefragment based on $\sigma(\langle E^\star/A\rangle)$ sufficient to reach the same types of final states. The contribution of FS = 3 or more fragments is much smaller than the other two and exhibit a $\langle E^\star/A\rangle$ dependence which is different from one reaction to the other, with $R_{FS\geq 3}(^{136}\text{Xe} + \text{p}) \ll R_{FS\geq 3}(^{136}\text{Xe} +^{12}\text{C})$ and a stronger slope with $\langle E^\star/A\rangle$ for ^{136}Xe + p. In the two-step picture, this must be interpreted as an insufficient prefragment selection with $\langle E^\star/A\rangle$ of the reaction channels leading to this type of final states, whose partial widths are therefore strongly dependent on other prefragment variables, essentially mass and charge of the prefragment as for TM .

The comparison of R_{FS} data with the models is shown in figs. 21 and 22, for ^{136}Xe + p and ^{136}Xe +^{12} C respectively. We see for the first reaction that the models basically agree between each other for the first two types of final states and that large differences appear for FS $\geq$ 3 fragment. $R_{FS=1}$ is fairly well reproduced by the models except at the highest $\langle E^\star/A\rangle$, where the models overestimate our data by a factor $\sim$ 2 by the models. $R_{FS=2}$ and $R_{FS\geq 3}$ are systematically and strongly underestimated, in particular at the lowest $\langle E^\star/A\rangle$. Such a discrepancy goes in the same direction as what is observed on the TM distributions, which are strongly underestimated at low TM.

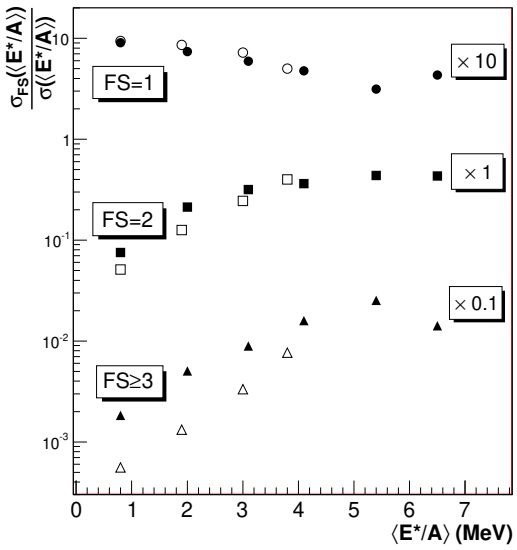

Figure 20: *Evolution of the content of the final states in fragments ($Z \geq 3$) with $\langle E^\star/A\rangle$ of ^{136}Xe + p (empty symbols) and ^{136}Xe +^{12} C (full symbols). Circles: FS=1; squares: FS=2; triangles: FS≥3. From the definition of R_{FS} in eq. 4, comes: $\sum_{FS} R_{FS} = 1$.*

These results follow in some sense the analysis of the reaction mechanism of ^{56}Fe + p at 1 GeV [8]. For this reaction we have indeed observed a good description of our data by GEMINI++ and by SMM to a lesser extent (both coupled with INCL). We have also seen that the statistical fragment evaporation model GEM [57], like the evaporation in the ABLA07 code is unable to reproduce the ^{56}Fe + p fragment production data, with a systematic large underestimate. But at variance with ^{136}Xe + p and ^{136}Xe +^{12} C, these models overestimate the fragment production at the lower $\langle E^\star/A\rangle$. This strengthens the necessity of a detailed study of fragment productions at relatively small $\langle E^\star/A\rangle$, both in models and experiments.

For ^{136}Xe +^{12} C, the theoretical predictions exhibit different behaviours from one model to the other. We can see in fig. 22 that the behaviour of R_{FS} with $\langle E^\star/A\rangle$ for FS $\geq$ 2

is not reproduced by the models. For FS = 1 only SMM is able to predict the measured $\langle E^\star/A\rangle$ dependence. Moreover, in the $\langle E^\star/A\rangle$ range of overlap between the two reactions, we observe that the predictions of GEMINI++ and ABLA07 differ from those of these models for ^{136}Xe + p, in contradiction with our data, whereas SMM's results are close. This is similar to the total-multiplicity observable (TM), even though multi-fragment final states contribute little to TM, which is dominated by the light-particle multiplicity. For $R_{FS\geq 3}$, the models predict a different behaviour from one reaction to the other but with a rather poor agreement with the data except perhaps for GEMINI++. As for the TM distributions we have tested the sensitivity of the model predictions to the different variables characterizing the prefragment at the end of the cascade phase of both reactions, but without being able to improve the quantitative agreement with the data on this observable.

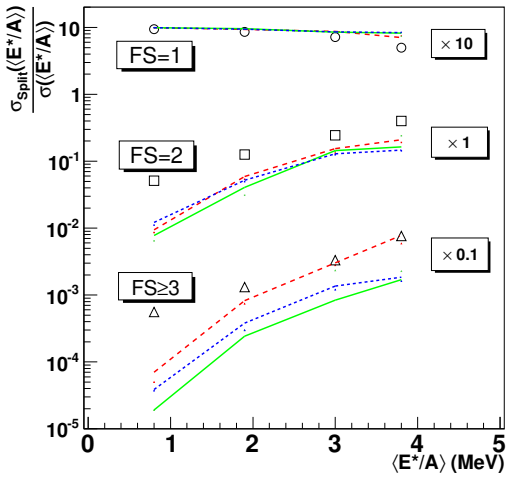

Figure 21: *Evolution of the content of the final states of* ^{136}Xe + p *in fragments* ($Z \geq 3$) *with* $\langle E^\star/A\rangle$ *compared with models:* ABLA07 *(solid green),* GEMINI++ *(dotted blue) and* SMM *(dashed red), coupled with* INCL. *Circles: FS=1; squares: FS=2; triangles: FS≥3. From the definition of* R_{FS} *in eq. 4, comes:* $\sum_{FS} R_{FS} = 1$.

VI. Conclusions

We have measured at GSI-Darmstadt two reactions with the SPALADiN setup ^{136}Xe + p and ^{136}Xe +^{12} C, at a primary beam energy of 1 GeV per nucleon. The combination of the inverse kinematics technique (^{136}Xe beam), of large-area detectors for the ions and the neutrons and of a large-acceptance magnet (ALADiN) makes our measurement very sensitive to particles and fragments of low kinetic energy in the centre-of-mass frame of the ^{136}Xe projectile, *i.e.* essentially to those produced in the decay of the excited projectile. We have performed a GEANT4 simulation of our experiment to determine the acceptance of the setup as a function of the particle charge and to compute the experimental filter for the comparison with theoretical models of the many-particle final states. We could estimate acceptances close to unity for the projectile's decay particles.

We extracted ion-production cross sections which we compared with existing data. For the ^{136}Xe + p, a good agreement with GSI-FRS data of Napolitani *et al.* [20] for the projectile residues ($Z \geq 30$) and a reasonable one for the lighter ions ($Z \leq 8$) were noted. In the light-ion range, a nice agreement was also found with data of Kotov *et al.* [42], an experiment performed in Gatchina at the same beam energy on p +^{nat} Ag, a system close to ours. Anyway, a significant disagreement between these FRS data and our measurement was seen in the range $Z \in [10, 30]$ which remains to be explained and should be the ground for a new experiment, preferentially with large acceptance detectors to avoid large corrections in the data analysis for the determination of cross sections. For ^{136}Xe +^{12} C, we observed a systematic normalisation difference of 30% of our data with an experiment done at LBNL by Binns *et al.* [9], but the charge dependences of the cross sections of both data sets are in agreement.

We analysed our data in the framework of the two-step model of ion-ion collisions in this energy range: A fast excitation of the inter-

acting nuclei based on intranuclear cascade, followed by a slower decay of the excited nuclear system. We worked essentially with the Liège cascade model INCL [26, 27, 28] and with three decay codes: ABLA07 [37], GEMINI++ [40] and SMM [41]. These models better described the ^{136}Xe + p data than the ^{136}Xe +^{12} C ones, in particular in the projectile residue range ($Z \geq 40$). It was noted that the disagreement between our data and those of [20] in the range $Z \in [10, 30]$ is of the same order as the dispersion between the models.

The measurement in coincidence and on an event-by-event basis of the final-state particles in both reactions permitted a detailed study of the reaction mechanisms. We have proposed a decomposition of the final states according to their content in neutrons, He nuclei and so-called "fragments" (of charge at least 3). Moreover, as was shown with our simulation, we could use the observable Z_{bound}, as first introduced by [6], as an indicator of the average excitation energy per nucleon $\langle E^\star/A \rangle$ of the prefragment at the end of the intranuclear cascade. We could demonstrate that the deexcitation of the prefragment, as we measure it, is dominated for both reactions by the evaporation of light particles (neutrons and He nuclei) on the whole $\langle E^\star/A \rangle$ range probed in our experiment. Moreover, we have seen that the total-multiplicity (TM) distributions of both reactions have very similar shapes as a function of $\langle E^\star/A \rangle$, giving strong hint to the two-step mechanism model used to analyze these data and an event selection based only on Z_{bound} / $\langle E^\star/A \rangle$. This close similarity was not explained by the models.

The domination of the prefragment deexcitation by evaporation channels for both reactions is fairly well reproduced by the models. Looking to the contributions of two- or more-fragment final-states to the cross section leads to a much more contrasted picture, the models being almost systematically well below our data for these channels. We have put forward a link with the description of the evolution of the TM distributions with $E^\star/A$, in particular their low-TM side, strongly underestimated by the models. We could show that this discrepancy between data and models is related to insufficient charge and mass losses of the target nucleus for a given $E^\star/A$ interval during the cascade phase as a function of the excitation energy per nucleon of the prefragment.

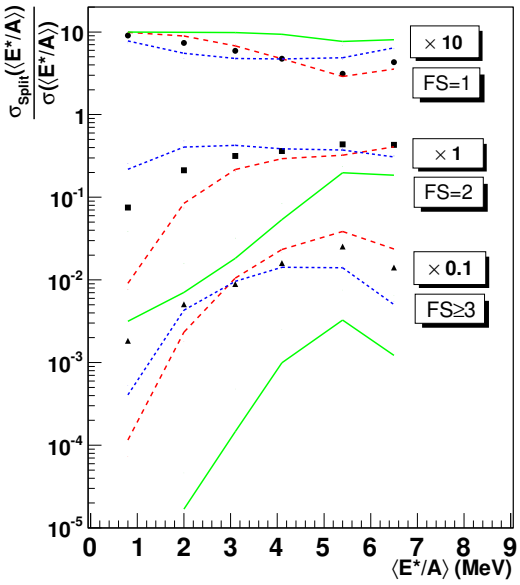

Figure 22: *Evolution of the content of the final states of* ^{136}Xe +^{12} C *in fragments* ($Z \geq 3$) *with* $\langle E^\star/A \rangle$ *compared with models:* ABLA07 *(solid green),* GEMINI++ *(dotted blue) and* SMM *(dashed red), coupled with* INCL. *Circles: FS=1; squares: FS=2; triangles: FS≥3. From the definition of* R_{FS} *in eq. 4, comes:* $\sum_{\text{FS}} R_{\text{FS}} = 1$.

Acknowledgements

The authors would like to thank Jean-Christophe David for useful discussions concerning the interpretation of the data and, for the support of this work, the EU-COST Action MP1208, the Bulgarian National Science Fund, contract No. DFNI-E02/6, the Slovak Scientific Grant Agency, contract 2/0121/14 and the Spanish Ministry of Science, contract FPA2010-22174-C02-02.

References

[1] S. Wang and the EOS Collaboration, *Phys. Rev. Lett.* **74**, 2646 (1995).

[2] W. G. Lynch, *Ann. Rev. Nucl. Part. Sci.* **37**, 493 (1987).

[3] The European Spallation Source, https://europeanspallationsource.se.

[4] H. A. Abderrahim *et al.*, *Nucl. Inst. Meth. A* **463**, 487 (2001).

[5] H. Geissel *et al.*, *Nucl. Instr. Meth. B* **70**, 286 (1992).

[6] J. Hubele *et al.*, *Z. Phys. A* **340**, 263 (1991).

[7] A. Schüttauf *et al.*, *Nucl. Phys. A* **607**, 457 (1996) and references therein.

[8] E. Le Gentil *et al.*, *Phys. Rev. Lett.* **100**, 022701 (2008).

[9] W. R. Binns *et al.*, *Phys. Rev. C* **36**, 1870 (1987).

[10] E. Le Gentil, *Doctorate Thesis*, University of Evry, France (2006).

[11] P. Chesny *et al.*, *SPALADiN target user and safety report* (2007).

[12] M. Pfützner *et al.*, *Nucl. Inst. Meth. B* **86**, 213 (1994).

[13] T. Gorbinet, *Doctorate Thesis*, University Paris-Sud, France (2011).

[14] P. Kreutz *et al.*, *Scientific Report GSI*, p. 213 (1988).

[15] J. Hubele *et al.*, *Scientific Report GSI*, p. 268 (1989).

[16] T. Blaich *et al.*, *Nucl. Inst. Meth. A* **314**, 136 (1992).

[17] W. Trautmann and the ALADIN 2000 Collaboration, *Int. J. Mod. Phys.* **E 17**, 136 (2008).

[18] C. Sfienti and the ALADIN 2000 Collaboration, *Phys. Rev. Lett.* **102**, 152701 (2009).

[19] P. Pawlowski *et al.*, *Nucl. Inst. Meth.* A **694**, 47 (2012).

[20] P. Napolitani *et al.*, *Phys. Rev. C* **76**, 064609 (2007).

[21] P. Napolitani *et al.*, *J. Phys. G* **38**, 064609 (2011).

[22] J. Jaros *et al.*, *Phys. Rev. C* **18**, 2273 (1978).

[23] R. K. Tripathi *et al.*, *Nucl. Inst. Meth. B* **129**, 11 (1997).

[24] GEANT4 collaboration, http://geant4.cern.ch.

[25] S. Agostinelli *et al.*, *Nucl. Inst. Meth. A* **506**, 250 (2003).

[26] J. Cugnon *et al.*, *Nucl. Phys. A* **352**, 505 (1981).

[27] A. Boudard *et al.*, *Phys. Rev. C* **66**, 044615 (2002).

[28] J. Cugnon *et al.*, *J. Korean Phys. Soc.* **59**, 955 (2011).

[29] D. Mancusi *et al.*, *Phys. Rev. C* **84**, 064605 (2011).

[30] A. Boudard *et al.*, *Phys. Rev. C* **87**, 014606 (2013).

[31] S. Leray *et al.*, *J. Phys. Conf. Series* **420**, 012065 (2013).

[32] D. Mancusi *et al.*, *Phys. Rev. C* **90**, 054602 (2014).

[33] J. D. Bowman, W. J. Swiatecki and C. F. Tsang, *LBNL Report*, p. 2908 (1973).

[34] D. J. Morissey *et al.*, *Phys. Rev. C* **18**, 1267 (1978).

[35] L. F. Oliveira *et al.*, *Phys. Rev. C* **19**, 826 (1979).

[36] J.-J. Gaimard and K. H. Schmidt, *Nucl. Phys. A* **531**, 709 (1991).

[37] A. Kelic *et al.*, *Joint ICTP-IAEA Advanced Workshop on Model Codes for Spallation Reaction*, p. 181 (IAEA, Trieste, Italy, 2008).

[38] J. B. Natowitz *et al.*, *Phys. Rev. C* **65**, 034618 (2002).

[39] R. J. Charity *et al.*, *Nucl. Phys. A* **483**, 371 (1988).

[40] R. J. Charity, *Phys. Rev. C* **82**, 014610 (2010).

[41] J. P. Bondorf *et al.*, *Phys. Rep.* **257**, 133 (1995).

[42] A. A. Kotov *et al.*, *Nucl. Phys. A* **583**, 575 (1995).

[43] V. F. Weisskopf and D. H. Ewing, *Phys. Rev.* **57**, 472 (1940).

[44] W. Hauser and H. Feshbach, *Phys. Rev.* **87**, 366 (1952).

[45] L. G. Moretto, *Nucl. Phys. A* **247**, 211 (1975).

[46] A. Sierk, *Phys. Rev. Lett.* **55**, 582 (1985).

[47] N. Bohr and J. A. Wheeler, *Phys. Rev.* **56**, 426 (1939).

[48] J. C. David *et al.*, *SATIF 10 Workshop Proceedings*, p. 273 (2011).

[49] S. Leray *et al.*, *J. Korean. Phys. Soc.* **59**, 791 (2011).

[50] IAEA benchmark of spallation models, http://www-nds.iaea.org/spallations.

[51] J. Alcántara-Núñez *et al.*, *Phys. Rev. C* **92**, 054602 (2015).

[52] C. Paradela *et al.*, *Phys. Rev. C* **95**, 044607 (2017).

[53] W. A. Friedman, *Phys. Rev. Lett.* **60**, 2125 (1988).

[54] W. A. Friedman, *Notas Phys.* **11**, 71 (1988).

[55] W. A. Friedman, *Phys. Rev. C* **42**, 667 (1990).

[56] D. Mancusi *et al.*, *Phys. Rev. C* **82**, 044610 (2010).

[57] S. Furihata, *Nucl. Inst. Meth. B* **171**, 251 (2000).